SIMULTANEOUS HST/XTE OBSERVATIONS OF SCO X-1

T. Kallman[1]

Laboratory for High Energy Astrophysics NASA/Goddard Space Flight Center

B. Boroson[2] and S. D. Vrtilek[3]

Harvard-Smithsonian Center for Astrophysics

Received __________________; accepted __________________

ABSTRACT

Sco X-1 is the brightest extra-solar point source of X-rays, and may serve as a prototype for low mass X-ray binaries as a class. It has been suggested that the UV and optical emission arise as a result of reprocessing of X-rays, and that a likely site for such reprocessing is an accretion disk around the X-ray source. If UV and optical emission are enhanced by reprocessing of X-rays, the X-ray variability may be manifest in UV emission: we test this by using high temporal resolution UV data obtained simultaneously with high temporal resolution X-ray data obtained simultaneously with the GHRS on the Hubble Space Telescope, and with the X-ray Timing Explorer (XTE). We analyze the variability behavior of the UV spectrum and of the X-rays, and we also measure the properties of the emission line profiles as viewed at high resolution (resolving power$\simeq$25,000) with the echelle gratings. The variability behavior does not provide direct support of the reprocessing scenario, although the correlated variability between UV and X-rays does not conflict with this hypothesis. Furthermore, the emission line profiles do not fit with simple models for disk emission lines.

Subject headings: stars: X-ray binaries

[1]email: tim@xstar.gsfc.nasa.gov [2]email: bboroson@riva.harvard.edu [3]email: svrtilek@cfa.harvard.edu

1. INTRODUCTION

X-ray binaries remain among the most fascinating astronomical systems. Pronounced periodic and aperiodic variability of the X-ray emission, on timescales ranging from milliseconds to decades, distinguishes the X-ray binaries from all other astronomical sources. For example, quasi-periodic oscillations (QPOs) in the X-rays from low mass X-ray binaries (LMXB's) (Lewin *et al* 1988; van der Klis, 1989) may help us understand accretion disks about compact objects near their Eddington luminosities, disk interactions with the magnetic fields of neutron stars, and pulsar evolution (e.g., Lamb 1988). Yet the current X-ray observations lack the ability to measure local physical conditions and dynamics with high-resolution spectrometry. In the optical and UV wavebands we can measure variability of the UV spectra of these sources on short timescales and at spectral resolution adequate to dissect accretion flows according to velocity. Thus, time-resolved UV spectrometry constitutes an important discovery space for these sources.

A prime target for such observations is Sco X-1, the first discovered and brightest extra-solar X-ray source and also the strongest LMXB UV source (Willis, et al., 1978). A prototype of the LMXBs, Sco X-1 consists of a neutron star and a low mass ($\leq 1 M_{\odot}$) secondary in a close ($\sim 10^{11}$ cm) 0.787d binary orbit (Crampton *et al.* 1976). Sco X-1 is one of two "Z-class" sources (displaying horizontal, normal, and flaring branches in the X-ray spectrum; see, e.g. Lewin and van der Klis, 1994, for a review) with an identifiable optical counterpart. The secondary (optical) star has a mass approximately 1 $M_{\odot}$; the spectrum shows emission lines due to H and He II and no recognizable absorption features; if the mass transfer is driven by stellar evolution, then the star is at or near end of its main sequence age (Cowley, 1976; Cowley and Crampton, 1975; Gottlieb, Wright, and Liller, 1975). The increase in QPO frequency as the source traverses the 'Z' shaped path in the X-ray color-color diagram has been intrepreted as being due to an increase in mass accretion rate. If so, the 'normal branch' QPOs are characterized by an inverse behavior between mass accretion rate and X-ray luminosity. More recently, Sco X-1 has been shown to be one of the sources of high frequency (kHz) QPOs (van der Klis et al., 1996; 1997).

The near-absence of stellar absorption features has slowed the interpretation of the optical and UV spectra of LMXBs. The mass transfer rates necessary to fuel the X-ray emission (assuming 10% efficiency), together with the stellar masses and orbital periods, suggest a similarity between LMXBs and high mass accretion rate cataclysmic variables (i.e. nova-like variables; Cordova and Mason, 1982). However, the optical and UV luminosities of LMXBs exceed those of CVs by factors 10-100. This suggests that most of the optical and UV luminosity ($L_{opt} \sim L_{UV} \sim 10^{-2} L_X$) comes from the accretion flow as it is illuminated by the X-rays from the neutron star.

The UV observations of Sco X-1 taken prior to September 1988 by the International Ultraviolet Observer (IUE) satellite have been summarized by us in an earlier paper (Kallman, Vrtilek, and Raymond, 1990, hereafter Paper I), and more recent IUE data by Vrtilek, et al. (1991). These data have been tested for variability associated with orbital motion, and for correlations among the various observables. The continuum spectra were found to fit to simple accretion disk atmosphere models which demonstrate that X-ray heating dominates the outer regions of the accretion disk. Correlations were found among the various emission line strengths, and upper limits to the emission line widths provided constraints on the location of the line emitting material if the emission is assumed to come from a Keplerian disk. IUE has shown that the UV emission line spectrum of Sco X-1 (Paper I; Vrtilek *et al.* 1991) is dominated by strong emission lines of C IV near 1550$\AA$ and N V near 1238$\AA$ and shows weaker lines of Si IV, O IV, O V, N IV, C III and less ionized species. The UV line strengths, ratios, and profiles vary noticeably ($\sim$ 20%) on the shortest timescales ($\sim$0.5 hr) that can be probed with IUE; but IUE does not have the time resolution to detect variability in the UV at frequencies higher than those corresponding to this timescale. If such frequencies were accessible observationally we could obtain information about the behavior of the accretion flow within the Roche lobe of the primary.

In spite of the effort devoted to understanding the X-ray variability behavior of LMXB's, little is known about their circumstellar environment and evolution. For example, estimates of the distance and reddening to Sco X-1 vary by a factor of 3 (Schachter et al., 1987; Willis, et al., 1980); secure distance estimates are vital to the understanding of the energetics of the X-ray emission. In addition, the X-rays and possible X-ray induced outflows from LMXB's are likely to affect the circumstellar environment by producing significant column densities of highly ionized species. Absorption studies, using Sco X-1 as a UV light source, can test for these ions. HST spectral resolution $\Delta V \sim 3\mathrm{kms}^{-1}$ (HRS Echelle A), enables the dissection of the circumstellar environment that X-ray, optical or IUE observations cannot do.

In this paper we describe the results of observations of Sco X-1 in the ultraviolet and X-ray energy bands carried out in February 1996 using the HST and XTE satellites. The goals of these observations are: (i) Search for UV variability on timescales shorter than those previously accessible. The X-ray variability behavior has been extensively studied, and the X-ray power spectrum is known to extend to $\geq$ 10 Hz during all of the variability states (e.g. Hasinger and Kurster, 1990). According to the reprocessing hypothesis the UV will reflect the variability of the X-rays on some timescales. For example, the accretion disk of Sco X-1 has a radius of about 2 lt-seconds so we expect that UV variability will be smeared on timescales much shorter than this; the UV emitting region should act as a "low pass filter" to the X-ray power spectrum. (ii) With HST, we can measure the interstellar column density toward Sco X-1 using interstellar Lα, thereby providing a third, independent distance estimate, which may help resolve the uncertainty. The interstellar line is broader than either the intrinsic Lα emission from Sco X-1 or the geocoronal line, and is apparent in the IUE spectra. (iii) Sco X-1 is likely to have an effect on any nearby interstellar medium. This can occur by X-ray photoionization, which will produce significant column densities of ions such as C IV and N V within a radius of ~3 pc (McCray, Wright, and Hatchett, 1976). These will have a detectable signature in high resolution observations as narrow features, with widths of $\sim 0.1\AA$. The relative strengths of such features provide a measure of the ionization balance in the interstellar medium, which in turn can constrain the density and X-ray flux history.

In what follows we describe our attempt to test some of these ideas using simultaneous observations of Sco X-1 by HST and XTE. In section 2 we describe the observations themselves; in sections 3 and 4 we discuss the spectral and timing analysis, respectively. In section 5 we discuss the results and summarize the conclusions.

2. OBSERVATIONS AND METHODS

2.1. HST Data

The data used in this analysis represents all of the available spectra of Sco X-1 taken by the Hubble Space Telescope (HST) during 29 February, 1996 using the Goddard High Resolution Spectrograph (GHRS; Brandt, et al., 1990). This was after the (first) HST refurbishment mission that installed COSTAR and repaired the side 1 electronics problem with the GHRS (Hartig et al., 1993). A description of the GHRS and gratings is given by Cardelli, Ebbetts and Savage (1990).

Sco X-1 was observed for a total of 6 satellite orbits with the GHRS. The grating/datamode combinations we used include: (i) the G140L (Energy (E) resolution $\Delta E/E$ ~150 km s^{-1}/c) grating in the wavelength region 1300 – 1580 $\AA$ (i.e. including both the Si IV λ 1400 and C IV λ 1550 resonance lines) for one satellite orbit in order to test for variability in the UV continuum and line strengths. Data was taken in RAPID Mode with data readout every 0.1s. Owing to limitations in the capacity of the tape recorders on HST the orbit was split into two separate exposures of approximately 1000 sec each, separated by a 9 minute interval in order to read the data to the ground. (ii) the G160M (Energy (E) resolution $\Delta E/E$ ~15 km s^{-1}/c) grating was used in the vicinity of the L α (1200-1233 $\AA$), N V (1220-1253 $\AA$) and C IV (1535-1568 $\AA$) lines (in ACCUM mode) for one satellite orbit each to measure the damping wings of the interstellar Lα absorption and hence the interstellar column, and to measure the profiles of the N V and C IV emission lines. (iii) the Echelle A grating (in ACCUM mode) was used in the vicinity of the N V λ1240 (order 45) and C IV λ1550 (order 36) lines for one satellite orbit each to search for narrow absorption components due to photoionized interstellar gas and a possible wind-blown bubble. For all gratings the Large Science Aperture was used, which has a field of view of 1.74$''$. A journal of observations is presented in Table 1.

The data analysis procedure consisted of extraction of flux-calibrated spectra, followed by continuum fitting and emission line fitting. No reddening correction has been applied to the data, although we do apply corrections as part of our fitting and interpretation procedure. The data were reduced in a uniform manner using the standard products produced by the HST analysis pipeline. In the case of the observations made in ACCUM mode these consist of the observed fluxes vs. wavelength, and errors vs. wavelength, corrected for flat field, with diode substeps added. We estimate a typical wavelength scale accuracy of 0.1 $\AA$ at 1300 $\AA$ for the G160M grating. The standard pipeline data reduction method was used. GHRS exposures were not taken in FP-SPLIT mode. A very useful property of the GHRS is that the random flux errors in the data are due simply to photon statistics and can be computed easily.

In the case of the RAPID mode data, flux and wavelength calibration are not performed as part of the standard analysis. Therefore, the absolute fluxes we derive are uncertain by as much as 10%. However, the primary goal of our analysis is to search for variability in the UV and we know of no instrumental effects which are likely to introduce spurious variability on short timescales. Furthermore, the field containing Sco X-1 is known to be free of other nearby sources which could potentially contaminate the UV spectra we observe (Sofia et al.,1969) . We use the large science aperture, which reduces the possibility of variability due to fluctuations in the satellite pointing direction. We therefore use the raw counting rates during the RAPID mode observations for our analysis of variability in the UV spectrum from Sco X-1.

2.2. XTE Data

Simultaneously with the HST observations, we observed Sco X-1 with the Rossi X-Ray Timing Explorer PCA (Bradt, Rothschild, and Swank 1993) continuously for 3459 seconds on 1996 Feb. 28. A maximum time resolution of 0.016 s (16 ms) was used throughout, although for much of the analysis discussed in Section 3 we binned the data to 1 s resolution for the sake of convenience. During these observations, an offset pointing of 0.5 degree was used, resulting in a counting rate of 6.3 $\times 10^5$ per 16 ms bin, or 3.94 $\times 10^7$ s^{-1}. We calculated power spectra of all 16ms data using 16 s data segments, and we calculated one average spectrum for each continuous data interval. This power spectrum clearly shows 6 Hz QPOs, characteristic of the horizontal branch QPOs which have previously been observed from Sco X-1 (e.g. Hasinger, 1986; Priedhorsky et al., 1986; van der Klis et al., 1985). Corrections for the PCA dead-time are not, as yet, sufficiently well understood to predict the Poisson component accurately. The conversion of the power in the QPO peaks to fractional rms amplitude depends on the derivative of the dead-time transmission function with respect to count rate (van der Klis 1989), which is currently unknown. The dead time is expected to suppress the QPO amplitude more than the total count rate. Our raw (i.e., uncorrected for dead time) fractional rms amplitudes are therefore lower limits to the true values. These could be several times as large.

3. SPECTRAL ANALYSIS

3.1. Continua

In order to make contact with previous observations of Sco X-1 (e.g. Willis, et al., 1980; Paper I; Vrtilek, et al., 1991), we begin by showing the time averaged G140L spectra. Figures 1a and 1b show the spectra in the two intervals of RAPID mode observations. These spectra show many of the features found in IUE spectra (Willis, et al., 1980; Paper

I; Vrtilek, et al., 1991): strong emission lines of C IV, Si IV, and other lines, and a strong continuum with an approximately flat spectral distribution. In order further to interpret these spectra, we present fits to the lines and continua using assumptions similar to those of Paper I.

The continua were fitted by first excluding the regions containing known strong emission lines from the reduced data (based on those detected in the IUE spectra in paper I), and then fitting to a model spectrum using a least-squares procedure. The model spectrum is the same as that used in Paper I. It is assumed to be that of an accretion disk and is given by:

$$F_\lambda^{model} = (4\pi D^2)^{-1} \int_{R_{in}}^{R_{out}} F_\lambda^{local}(T(R)) 2\pi R dR \tag{1}$$

where R is the disk radius, $T(R)$ is the disk photospheric temperature, F_λ^{local} is the local spectrum radiated by the disk surface, R_{in} and R_{out} are the disk inner and outer radii, respectively, and D is the distance to Sco X-1. We ignore emission from the X-ray heated face of the companion star. This has been shown to be a very minor contribution to the UV light in the low mass X-ray binary Cyg X-2 (Vrtilek et al., 1990), and Sco X-1 (Vrtilek et al., 1991; Paper I), although it appears to be a significant contribution in the Her X-1/HZ Her system (Howarth and Wilson 1983). As discussed in the following section, we are unable to detect the orbital modulation which would be expected from a heated companion in the data considered here. Furthermore, we expect an illuminated companion more nearly to resemble a single temperature black-body or stellar-type distribution, significantly different from the disk spectral distribution; our success in fitting to disk spectra provides *post hoc* justification for neglect of companion star heating.

Theoretical calculations of the local disk spectrum are affected by the various and uncertain heating mechanisms which may affect the disk atmosphere (see, e.g. Shaviv,

1989) and by the problems of line blanketing and non-LTE conditions familiar from the modelling of stellar atmospheres. In the absence of detailed models for the continuum spectra emitted by accretion disk atmospheres there are two plausible choices for F_λ^{local}: normal stellar atmospheres or black-body distributions. Studies of cataclysmic variables have shown that neither of these distributions closely matches observations of CV accretion disks in detail (Wade 1984). Many of the differences between these two cases, and their effects on the total disk spectra have been discussed by Vrtilek, et al. (1990), who adopt stellar atmospheres in their fitting of the spectra of Cyg X-2. In our models we follow Vrtilek et al. (1990) and adopt the stellar atmospheres from the compilation by Kenyon (1989) when calculating F_λ^{local}. For the purposes of modelling the UV continuum the inner optically thin or Compton-scattering dominated regions of the disk are unimportant (Shakura and Sunyaev, 1972; Eardley, Lightman, Payne and Shapiro, 1978).

The disk temperature distribution may be influenced by a variety of factors, including the viscous release of energy by the accreting material and heating by X-rays from the central compact object. Viscosity alone produces a temperature distribution $T_{acc}(R) = (3GM\dot{M}/8\pi\sigma)^{1/4}R^{-3/4}$, where M and $\dot{M}$ are the central compact object mass and mass accretion rate, respectively. X-ray illumination produces a temperature distribution $T_x(R) = (L_x f_x/(4\pi\sigma))^{1/4}R^{-1/2} = (\dot{M}c^2\eta f_x/(4\pi\sigma))^{1/4}R^{-1/2}$, where L_x is the X-ray luminosity and η is the accretion efficiency, which we assume to be 0.1. The illumination of the disk by X-rays is parameterized by the factor

$$f_x = (4\pi R^2 F_{x,inc})/L_x \tag{2}$$

the ratio of the X-ray flux incident on the disk surface, $F_{x,inc}$ to the total available unattenuated X-ray flux at that radius. The quantity f_x may be regarded as analogous to the 'Eddington factor' familiar from the study of stellar atmospheres. If the X-rays are unattenuated and streaming radially outward from a point source at the center of the disk then f_x=sinθ, where θ is the local flaring angle of the disk. On the other hand, if the X-rays are nearly isotropic with the corresponding mean intensity, $f_x \simeq 1$. There is no *a priori* reason to adopt either of these scenarios, since there is evidence that the disks in low mass X-ray binaries are surrounded by X-ray induced coronas (Begelman and McKee, 1982; Begelman, McKee and Shields, 1982; White and Holt, 1982). Such coronas will have temperatures $\sim 10^7$ – 10^8 K and optical depths to electron scattering 0.1 – 1, and so can isotropize the X-rays illuminating the disk. The detailed properties of such a corona, including its radial extent, are somewhat uncertain, although the models of London (1984) suggest that $f_x \leq 10^{-1}$ for accretion onto a neutron star at a rate less than the Eddington limit.

A consequence of the different temperature dependences of the disk temperatures produced by accretion and X-ray heating, and of the great range of radii spanned by likely disk models, is that X-ray heating is likely to dominate viscous heating at large radii, i.e. $R \geq R_{eq} = 3GM/(2f_x\eta c^2)$ =2.2 $\times$ 10^9 cm $(\eta/0.1)^{-1}(M/M_\odot)(f_x/10^{-3})^{-1}$. Thus, even for very small values of f_x, X-ray heating can determine the temperature at large radii, and can strongly affect the UV continuum.

The integrated spectrum given by equation (1) will be influenced by the sum of the local spectra from the various disk radii at wavelengths less than those which characterize the outer disk radius, $\lambda_{out} \sim hc/(k \max(T_x(R_{out}), T_{acc}(R_{out})))$. If so, a disk which radiates locally as a black body will have $F_\lambda \sim \lambda^{-7/3}$ if viscous heating dominates and $F_\lambda \sim \lambda^{-1}$ if X-ray heating (with f_x constant across the disk surface) dominates. Stellar atmosphere spectra are generally flatter than black body spectra at the corresponding temperature. For $\lambda \geq \lambda_{out}$, the spectrum has a Rayleigh-Jeans slope, $F_\lambda \sim \lambda^{-4}$.

In evaluating the model spectrum we assume that Sco X-1 is a 1.4 $M_\odot$ Eddington limited neutron star emitting X-rays at L=1.9×10^{38} erg s^{-1} (the Eddington limit for 1.4 $M_\odot$), implying a distance D=2 kpc, (Vrtilek, et al., 1991). We take the accretion efficiency η=0.1, so that $\dot{M} \leq 1.9 \times 10^{18}$ gm s^{-1} (corresponding to $3.05 \times 10^{-8} M_\odot$ yr^{-1}. The free parameters used to maximize the fit to the observed spectrum include f_x (assumed to be constant over the disk surface), the mass accretion rate, and the disk outer radius, R_{out}. The observed spectrum was dereddened using the Savage and Mathis (1988) reddening curve and E(B-V)=0.3 (c.f. Paper I), i.e. we multiply the observed flux by the factor $10^{y\mathrm{E(B-V)}/2.5}$, where y is obtained by interpolating the Savage and Mathis curve at the desired wavelength. The mass accretion rate is constrained to be less than the Eddington limit, i.e. $\dot{M} \leq 1$ (in units 1.9×10^{18} gm s^{-1}); when this limit is reached X-ray heating is the dominant energy source for the UV emitting part of the disk. Also, we constrain the disk outer radius to be less than 1 (in units of 2 light-seconds, 6×10^{10} cm); this is the most probable outer radius found by Vrtilek et al. (1991). The values of f_x for the two G140L spectra are 3.39E-03 and 2.45E-03, together with the limiting values for $\dot{M}$ and R_{out} provide adequate fits to the data. The spectral slope in the UV is flatter than $F_\lambda \sim \lambda^{-7/3}$ behavior expected for viscous dominated disks. This is consistent with the effects of X-ray heating, but is partially offset by the fact that the UV is affected by the Rayleigh-Jeans turnover at λ_{out} ~7000$\mathring{A}$. We emphasize that the continuum fitting results provide strong evidence for a disk heating source in addition to viscous dissipation. If X-ray heating were not occurring, then a viscous disk with a mass accretion rate corresponding to the observed luminosity would fail to account for the observed UV flux by a factor $\simeq$16. The average dereddened UV flux in the bandpass of the G140L (1260$\mathring{A}$–1550$\mathring{A}$) grating is $F_\lambda \simeq 3 \times 10^{-12}$ erg cm^{-2} s^{-1} $\mathring{A}^{-1}$, corresponding to a UV luminosity of 10^{36} erg s^{-1} if the distance to Sco X-1 is 2 kpc. Although this is uncertain by a factor of $\simeq$2 owing to uncertainties in the reddening correction (see below), it still is much greater than that observed from the most luminous cataclysmic variable. This may be compared with the observed flux in the 2-10 keV X-ray band as observed by XTE of 4.8×10^{37} erg s^{-1} (see below).

3.2. Lines

3.2.1. *Low Resolution Time-Averaged Spectra*

Clearly apparent in Figure 1 are the strong emission lines of C IV $\lambda\lambda$ 1548, 1550, Si IV $\lambda\lambda$1394, 1403, O V λ 1371, and O IV λ 1339, 1344. In addition there are indications of other weaker features at 1482 and 1500 Å, possibly due to O I or S I (e.g. Morton and Smith 1973). We defer a discussion of the absorption lines to a later section.

Emission line strengths were extracted by fitting the dereddened spectra in the vicinity of emission lines to a linear continuum plus a gaussian line or blend of (two) lines. This procedure was carried out for each individual image and for the averaged spectra for the obvious strong lines: N V λ1240, O V λ1370, Si IV λ 1400, and C IV λ1550. This procedure allows for the doublet structure of the Si IV and N V lines. H Lα was fitted together with the fits to N V λ1240. We have not included continuum absorption in our fits to any of the lines; a measure of the validity of this assumption can be obtained from the results of fitting to the high resolution data in the later sections. Table 2 presents the line fluxes (in units of 10^{-11} erg s^{-1} cm^{-2}), equivalent widths (in Å), and the fractional errors (1 σ) associated with these quantities.

The G140L grating lacks sufficient spectral resolving power to allow us to measure the widths of features less than ~100 km s^{-1}, but we can set limits on the widths of these features. This situation is similar to the results from the various IUE low resolution observations of Sco X-1 (Paper I; Vrtilek et al., 1991), in which widths were less than the resolution of the IUE low resolution short wavelength instrument. However, we also clearly detect variability in the spectrum, both lines and continuum, in the ~ 30 minute interval separating the G140L observations. This is apparent from the differences in the fitting parameters for both the continuum and the lines in in table 2, and from Figure 1, in which the interval 1 spectrum (dashed curve) is overlayed onto the interval 2 spectrum (solid curve) in the lower panel. This variability is comparable to the shortest timescale variability which had previously been sampled using IUE.

3.2.2. Medium and High Resolution Data: Emission Lines

We now discuss the results of the higher spectral resolution observations taken in ACCUM mode. Tables 3 and 4 show the results of fitting the line profiles obtained using the G160M and echelle gratings. These fits were performed separately for each line doublet, for each grating, and for each assumed line shape. The statistically significant differences between the G160M and echelle fits, therefore, we attribute to intrinsic variability in the lines. The errors are the 90% confidence limits obtained by the criterion described by Cash (1978). Figures 8-10 show comparisons of the fits (solid curves) with the data (crosses). Clearly apparent in the observed profiles of C IV and N V are the doublet components at 1238.821 and 1242.804 $\AA$ and 1548.202 and 1550.774 $\AA$, respectively. Also apparent, particularly in the echelle spectra (Fig. 10), are the doublet components of the interstellar absorption lines of the corresponding resonance lines. Furthermore, the absorption wavelengths are offset from both the peak wavelengths of the emission lines, and from the laboratory wavelengths. The numerical values of the offets of the absorption lines and the peaks of the emission lines from the laboratory wavelengths are given in the tables.

We have tried two different trial shapes in fitting to the emission line profiles. The first is a Gaussian, which corresponds crudely to the shape expected from an isothermal gas, or from a turbulent medium with a velocity distribution which mimics a thermal distribution. In this case, the free parameters are the normalizations, widths, and centroids of the various emission features. We fit each observation separately, and allow the normalizations of the various lines within each spectrum to vary independently. We find in all cases acceptable fits to gaussian line profiles for the various lines. The centroids are offset from the laboratory wavelengths by -78 – -177 km s^{-1} (i.e. blueshifted), and the widths are 270 – 350 km s^{-1}. We also are able to measure the ratio of the doublet components (1548Å/1551Å for C IV and 1237Å/1242Å for N V), which we find to be 1.2±0.1 and 1.1±0.2 for the C IV (Fig. 8) and N V (Fig. 9) echelle observations, respectively. The offsets are similar to those measured by Crampton et al. (1976) for the Balmer lines, which suggests comparable contributions from orbital motion and from the systemic velocity of Sco X-1.

The second trial shape is a disk line, in which the broadening of the line is assumed to be dominated by Keplerian motion in a disk. In this case the free parameters for each line are the central wavelength, the outer radius of the disk, and the distribution of line emissivity per unit area with radius. This last quantity we parameterize according to a power law distribution, i.e. $F(R) = F_0(R/R_0)^{-\gamma}$, where we choose the fiducial radius, R_0, to be the innermost radius of the disk, R_{in}, and F_0 is the emissivity per unit area there. Clearly this formulation can be at best a crude representation of a real disk, in which the line emissivity must depend on factors such as the distribution of illumination or mechanical heating with radius.

The most obvious and striking prediction of the disk line model is that, for $\gamma \leq 2$, the profile will have a minimum flux near the central wavelength, and there will be two peaks of equal strength offset from the center of the line by an amount corresponding to the Keplerian speed at the outer disk edge (if $\gamma \geq 2$, the profile will be flat, or will have peaks at the maximum shift from line center; we discount this possibility in the remainder of our discussion). For a disk surrounding a 1.4 $M_\odot$ object, the speed of a Keplerian orbit at $\sim 6\times 10^{10}$ cm from the object is 556 km s^{-1}. Such structure should be easily resolvable with either the G160M or the echelle gratings, and it is not apparent in the data from Sco X-1. The only possible scenario under which the disk line model could be considered is if the separation of the two peaks is such that one of the peaks coincides with the interstellar absorption, thereby rendering the appearance of the line to be single peaked. Since the separation in velocity of the emission and absorption is $\sim$ 100 km $^{-1}$, such a scenario requires separation of the emission peaks which is considerably less than expected for a disk with outer radius $\sim 6 \times 10^{10}$ cm. In what follows we illustrate the possibility of disk line fits by using a disk outer radius R_{out}=2.5 $\times$ 10^{11} cm and an inclination sin(i)=0.32. This radius is comparable to the best estimates for the binary separation (Crampton et al., 1978), and is therefore greater than the likely outer radius of the disk (the "Paczynski-Smak radius"; e.g. Frank, King and Raine, 1985). In spite of this fact, we show in Figures 8 and 9 and in table 4, the results of our attempts to fit disk line profiles to the echelle spectra. The free parameters used in these fits are: γ (the power law dependence of line emissivity with radius), the line centroid wavelength, and the normalization for each component. We use an automated procedure to fit for these quantities, together with the values of R_{out}=2.5 $\times$ 10^{11} cm and sin(i)=0.32 given above. As shown in figures 8 and 9, we obtain acceptable fits to the echelle data from these fits, although the χ^2 values are larger than those for the gaussian fits.

3.2.3. Medium and High Resolution Data: Absorption Lines

The fitting procedures described in the previous subsection yield the strengths and widths of the narrow absorption components seen in the echelle spectra of figures 8 and 9. The parameters of these lines are listed in tables 3 and 4. It is clear that these lines are offset from the expected laboratory wavelengths by amounts ranging from -26 – -40 km s^{-1}, i.e. by amounts less than are the emission components. The required widths imply turbulent or thermal velocities 30 – 40 km s^{-1}. These are greater than the $\simeq$4 – 15 km s^{-1} expected from a thermal gas near 10^4 – 10^5 K. The equivalent widths correspond to line center optical depths of 1 – 3 for the stronger doublet component, although these values differ somewhat depending on the assumed shape for the emission component, and are systematically lower for the G160M spectral than for the echelle spectra.

3.2.4. The Lyman α Line

Figure 10 shows the G160M spectrum in the vicinity of the Ly α line. Clearly apparent are the central emission component and the broad absorption due to interstellar material. The central emission component is likely to be dominated by the geocoronal background. However, the GHRS aperture is small enough that this makes a negligible contribution to the flux more than $\simeq$1 $\AA$ away from line center. We have fitted this spectrum to a Gaussian emission plus absorption by a Voigt profile. Free parameters are: the emission component central wavelength, width, and normalization, and the Doppler and damping parameters and optical depth of the absorption. As was done for the fits to other lines, we assume a linear continuum across the spectral band of the instrument. The results of the fit are as follows: v_{0emiss} = 19.5$\pm$1.5 km s^{-1}, σ_{emis} = 72.05$^+$0.79$_-$0.94 km s^{-1}, EW$_{emis}$=5.4+$_-$0.34$\AA$, v_{0abs} = 74^{+9}_{-40} km s^{-1}, τ_{abs} = 9.07$\pm$0.30 $\times$ 10^8. We fix the Doppler parameter and the damping parameter at the values expected for a 100 K gas: $v_{thermal}$ = 1.3 km s^{-1}, $a = \Gamma/(4\pi\Delta\nu_D) = 4.65 \times 10^{-3}$. The derived optical depth corresponds to an H I column density N_{HI} = 8.9$\pm$0.3 $\times$ 10^{20} cm^{-2}. This is compatible with the value derived in Paper I ($\leq 1\sigma$) owing to the large statistical errors and the much greater contamination by geocoronal Lyα in the IUE data. We can estimate the contribution of geocoronal Lα to our data away from line center, using the known flux and the aperture of the instrument; the counting rate is predicted to be 0.02 counts sec^{-1} diode^{-1} (Ake, 1996) near 1220 $\AA$, corresponding to a total flux 4×10^{-15} erg s^{-1} cm^{-2} $\AA^{-1}$ (Ake, 1996). This value is comparable to the error bars already assigned to the flux at this wavelength, so we feel confident that the geocoronal line makes only a minor contribution to the detected flux. In fact, we have experimented with subtracting this value from the measured spectrum and then fitting the line, and we find that the derived line values differ from those cited above by much less than the quoted errors.

Combining with the relation from Diplas and Savage (1994) between UV reddening and HI column we would predict $E(B-V)$=0.18$\pm$0.0061. This is less than the value inferred in Paper I and by Willis et al. (1978) of $E(B-V)$=0.3, and is similar to that suggested by Schachter, et al. (1989). However, there are significant uncertainties associated with measuring the H I column by fitting the 2200$\AA$ feature using IUE data, so that we do not consider the quantities obtained here to be inconsistent with those from Paper I and from Willis et al. (1978). Furthermore, uncertainties in the mean density and in the homogeneity of the interstellar gas along our line of sight to Sco X-1 mean that this reddening value does not necessarily imply a distance much less than $\sim$1.5 kpc, as suggested by Knude (1989). Recent VLBA observations have limited to the trigonometric parallax to Sco X-1, and set a lower limit of 1300 pc on the distance (Bradshaw, Fomalont, and Geldzahler, 1997). This is consistent with the hypothesis that Sco X-1 is Eddington limited, and that the observed absorption and reddening are indicative primarily on the density of neutral hydrogen and dust along the line of sight, rather than the distance.

4. TIMING ANALYSIS

4.1. Variability

Figure 2 shows lightcurves from the RAPID mode data, binned into 10 second bins. Panel (a) is the flux in the vicinity of the C IV line, in the wavelength range from 1537 to the longest wavelength accessible to the G140L grating, approximately 1550 Å. Panel (b) is the flux in the total UV band spanned by the G140L grating, and panel (c) is the X-rays, integrated over the entire XTE bandpass. All count rates are in counts per 10 second bin. Time is measured in seconds from the beginning of the X-ray observations. The extent of the overlap between the X-rays and the two intervals of UV observations is clear from this figure. Owing to the absence of flux calibration in these data it is likely that this effect is due to gain drifts associated with changes in conditions during the satellite orbit. Therefore, in what follows we have removed this trend in the data by subtracting a linear fit to the mean counting rate in both the UV wavelength bands shown here. As we will show, the residual flux shows variability on timescales much shorter than those associated with the satellite orbit, and which therefore are not likely to be associated with gain changes in the GHRS.

The mean counting rates and fluctuations associated with the data in figure 2 are as follows: In the C IV line the mean counting rate is 124.6 s^{-1} for the first observation interval, 104.5 s^{-1} for the second interval. In the continuum the rates corresponding quantities are 1773 s^{-1} and 1403 s^{-1}, respectively, while in the X-ray band the counting rate is 6.384×10^5 s^{-1} during the entire interval shown in figure 2. As a comparison, the fractional rms variation we derive from the various observed datasets (using the definition given by Lewin, Van Paradijs and Van der Klis, 1989) is 0.45, 0.49, 0.089, 0.090, and 0.0021, for the two line intervals, the two continuum intervals, and the X-rays, respectively, Since the errors are dominated by counting statistics for all of these data, the signal to noise ratio is $\simeq 1 - 1.5$ for all the observations on the shortest timescales, assuming that most of the variance occurs on these timescales.

More detail about the variability is shown in the power spectra, in Figure 3. Panel (a) shows the spectrum in the C IV line, panel (b) in the UV continuum, and panel (c) in the X-rays. Panels (a) and (b) here represent the average between the two G140L observation intervals; all have been binned onto evenly spaced logarithmic frequency intervals, and the error bars shown represent the dispersion in the values within that interval. The normalization has been chosen according to the prescription of Leahy et al., (1983), with the consequence that noise due to counting statistics has a level of 2. Panel (a) shows a clear excess of power, by a factor $\sim$3, at frequencies below $\sim$ 0.1 Hz (i.e. timescales $\geq$10 seconds), relative to the noise level. In the UV continuum and X-rays this same behavior is apparent, and the excesses are factors of $\sim$100, and 5×10^3, respectively. This shows that there is a clear excess in variability in all the datasets at low frequencies, relative to the noise level predicted by counting statistics, in contrast to the estimates in the previous paragraph. We have also examined the UV power spectra from the two intervals of data separately. The power spectra show a $\simeq$ 20% difference in the power level of the low frequency noise between the two intervals, with no detectable difference in the shape or high frequency behavior between the two.

The X-ray power spectrum shows a clear detection of power at all frequencies, above that expected from noise alone. Although we restrict ourselves here to frequencies accessible to both the HST and XTE instruments, the XTE data extends to frequencies $\simeq$60 Hz with adequate statistics to detect power at all frequencies. Such spectra show clear $\sim$6 Hz QPOs, demonstrating that Sco X-1 was on the normal branch during our observations. Fits to the observed spectrum indicate a flux in the 2-10 keV band of 1.08×10^{-7} erg cm^{-1} s^{-1} averaged over the entire interval shown in figure 2.

Figure 4 shows the autocorrelation functions (ACF) for the various light curves: the C IV line (panel a), the entire UV band (panel b), and the X-ray band (panel c). It is clear that the UV continuum and X-ray datasets have correlated variability around zero lag. Here and in what follows the various correlation functions are calculated using the definitions and the subroutines of Press et al. (1986), i.e., the the discrete correlation function of two time series $g(t)$ and $h(t)$ is

$$\mathrm{Corr}(g,h)_j \Longleftrightarrow G_k H_k^*$$

where $g_j \Longleftrightarrow G_k$, $h_j \Longleftrightarrow H_k$ H_k^* is the complex conjugate of H_k and $\Longleftrightarrow$ denotes a discretely sampled Fourier transform pair. The correlation functions are also normalized by dividing by the geometric mean of sums of the variance of each member; this is the normalization adopted by Leahy, et al., (1983).

The fractional amplitudes of the zero lag modulation are 28% and 7%, respectively, for the two datasets. The full width at half maximum of the X-ray ACF is $\simeq$ 150 sec, and is indicative of the excess power in the X-rays at frequencies less than 0.1 Hz. The full width at half maximum for the UV continuum is considerably greater, $\sim$300 s, and is likely to be affected by the window function introduced by the $\simeq$1000s observation intervals.

Figure 5 shows the cross correlation functions (CCFs) of the various datasets: UV line vs. X-ray, UV continuum vs. X-ray, and UV line vs. UV continuum. In this case the cross correlations between the X-rays and the two intervals of UV data were calculated separately and then averaged. Apparent in these figures are significant negative correlations at positive lags (UV relative to X-rays) of approximately 100 sec in the UV vs. X-ray panels. The amplitude of this anticorrelation is -0.05. The apparent sharp rise in cross correlation at larger positive lags, and the residual negative correlation at smaller lags, are consistent with the effects of the window function and counting statistics (as demonstrated in the next section).

We consider this convincing evidence for (anti) correlated variability, and for a detectable lag between the X-ray variability and the UV continuum. The cross correlation of X-rays with the UV line does not have sufficient statistical significance to allow similar inferences to be drawn (the minimum between 50 and 100 second lag is approximately 1σ) although there is no obvious indication that the UV line and continuum differ in their variability. Complementary evidence of this comes from the cross correlation of the UV line and continuum, which resembles the autocorrelation functions of the two UV datasets. This is consistent with no detectable variability of the ratio of lines to continuum.

Fundamental to the reprocessing model for UV emission is the assumption that the UV and X-rays are connected by an integral equation. If this equation is assumed to be linear, then the kernel, also known as the response function (Blandford and McKee, 1979), can in principle be obtained by inverting the equation in Fourier space. This procedure has been discussed at length in the context of active galactic nuclei (e.g. Edelson and Krolik, 1988; Krolik and Done, 1995; Done and Krolik, 1996; and references therein), and is subject to some uncertainty owing to the fact that such inversion procedures inevitably introduce noise into the result. We have attempted to apply this procedure to our data using the technique of regularized linear inversion (Krolik and Done, 1995; Done and Krolik, 1996), using a computer code kindly supplied by J. Krolik. This procedure requires the introduction of a default model for the response function, which we have taken to be constant as a function of lag. Another parameter which affects the results of this procedure is the ratio of the importance of χ^2 relative to the regularization condition; we find that a value of 0.05 for this parameter gives an acceptable value χ^2=24.7. An advantage of this procedure over others which have been used to solve similar problems is that it provides a relatively straightforward estimate of errors. Figure 7 shows the response function obtained by this procedure, together with the estimated errors as a function of positive lag. This clearly shows the same features of both the observed and simulated cross-correlation functions: a negative response between UV and X-rays near 100 seconds lag, together with an increase at larger lags. These features are statistically significant (the depth of the minimum differs from the value at zero lag by 2.5 σ) and provide further confirmation of the results of the previous sections.

4.2. Simulations

In order better to understand the variability in both UV and X-ray, and the correlated behavior, we have simulated the data using shot noise models. For the X-rays, these are chosen for the purpose of convenience; we do not regard them as necessarily being a plausible physical model for the variability. Rather, they adequately reproduce the gross features of the power spectrum and the autocorrelation. Therefore they serve as a convenient driving function for use in probing the correlated UV variability. The shot noise model we adopt has exponential shots, with characteristic decay time 100 seconds. The shots are generated randomly in time according to a Poisson distribution with characteristic interval 1 s^{-1}. In addition, there is a component which we model as being constant in time. The relative contribution of shot component and the non-shot (constant) component to time series is 30:1. The time series produced by these two components is also modified by the addition of noise associated with counting statistics. Since the signal to noise ratio of the X-ray time series is very large, counting statistics have a negligible effect on the power series, ACF, and CCF. However, in order to account approximately for the X-ray variability at the highest frequencies of interest here, we have artificially amplified the noise by a factor of 5 relative to what would be produced by counting statistics alone.

Using this simulated X-ray time series we obtain a power spectrum which resembles the observed spectrum in its overall shape, and agrees in the magnitude of the power to within a factor of 2. The long shots have the effect of producing the relatively large power observed in X-rays at frequencies less than 10^{-2} Hz, while the amplified noise produces the power observed at higher frequencies. The simulation succeeds in reproducing the exponential falloff of the autocorrelation function for lags less than about 200 s. This is apparent from the third panel of Figure 6.

The key goal in constructing these simulations is modelling the UV power spectra and correlation functions. In doing so, we have tried various possible assumptions about the UV response to X-rays. These include: uncorrelated UV variability, correlated UV variability with no lag, correlated UV variability with a lag (possibly negative), and anti-correlated UV variability with or without lags. Discussion of these is simplified if we refer to them according to simple mnemonics: C, U, and A refer to correlated, uncorrelated, and anticorrelated, respectively, and L and N refer to lagged and unlagged.

Although we will not display here all the results of such experiments, we will briefly describe some of the conclusions, many of which are obvious in retrospect. First, simulated UV power spectra assuming a pure secular decrease in the flux, plus counting statistics, can reproduce the observed power spectra shown in Figure 3. This corresponds to model UN in the notation of the previous paragraph. However, such simulations do not adequately reproduce either the autocorrelation or UV-X-ray cross corrrelations. Instead, we model the UV timeseries as the sum of two components: one which is constant in time, and one which responds to the shot noise component of the X-rays (with an amplitude which may be negative), and which may be lagged relative to the X-rays. The relative contributions of these two components to the UV lightcurve is set by the amplitude, which we denote A. The count rate obtained in this way is then corrected for the effects of noise due to counting statistics, again assuming that the noise follows a Gaussian distribution. For A=0, the UV lightcurve will therefore be pure noise at the observed mean counting rate (model UN). For $A<0$ there will be additional variable component which will be anticorrelated with the shot noise part of the X-rays (model AN), and for $A > 0$ the UV and X-rays will be correlated model (model CN).

Following the results of the previous section, we take A=-0.04, and assume a lag of 100 s. This corresponds to model AL in the above notation. The cross correlation produced by this simulation is shown in Figure 6. Although the detailed shapes differ from the observed data, this figure does reproduce the gross features of the observed CCF, namely the negative correlation near 100 s, relatively constant values at smaller lags, and the steep rise at longer lags. Experiments verify that the strength and location of the 100s feature are directly proportional to the values of A and lag time used in the simulation. Also, the behavior at larger positive lags is similar to that observed, and experiments show that this depends solely on the window function for the observations. The width of the 100s feature is narrower than observed (40 ± 10 s. in the simulation, FWHM, vs. 110 ± 30 s. in the data), suggesting that there is additional short timescale variability in the UV which we have not adequately modelled. However, the qualitative agreement between the observed and simulated CCFs confirms the existence of lagged, anticorrelated variability between the X-ray and UV continuum. The other models fail to account for the minimum in the UV continuum/X-ray anticorrelation at 100 second lag; model CL produces a maximum rather than a minimum, and models UL and UN produce no features in the CCF.

5. Discussion

The cross correlation between UV and X-rays provides evidence for inverse behavior between the X-rays and the UV lines and continua. This contrasts with the simplest reprocessing models, in which the lines and continua arise from an X-ray heated accretion disk atmosphere. Such a scenario would predict a positive correlation between X-rays and UV, with a lag associated with the combined effects of light travel time across the disk and the local timescale for reprocessing to occur on the disk surface. Plausible values for these timescales are ∼1 s and ∼10 s (London and Cominsky, 1984), respectively. The signal to noise ratio in our data is too large to detect correlated variability on these timescales, so we cannot rule out the validity of this scenario. Furthermore, the energetic arguments in favor of reprocessing remain valid, and so we favor models for Sco X-1's UV production in which reprocessing remains the primary mechanism.

The inverse behavior we observe on longer timescales suggests that increases in the X-ray luminosity impede production of UV photons, with a lag of approximately 100 seconds. This could occur either when X-rays ionize the gas in the accretion disk atmosphere to a level where it emits UV with low efficiency, or by affecting the disk structure so that a small fraction of the X-rays are intercepted by the disk. In either case a requirement is that the timescale be comparable to the observed lag. The timescale which affects reprocessing on a microscopic scale is the photoionization timescale, which can be written $t_{phot} \simeq 2 \times 10^{-3} \varepsilon_{10}^{-1} R_{11}^2 L_{38}^{-1} \sigma_{20}^{-1}$ s, where ε_{10} is the mean ionizing photon energy in units of 10 keV, R_{11} is the distance from the X-ray source in units of 10^{11} cm, L_{38} is the X-ray luminosity in units of 10^{38} erg s^{-1}, and σ_{20} is the photoionization cross section in units of 10^{-20} cm^{-2}. This is likely to be short compared to the observed lag, and the corresponding heating time is shorter still. The timecale for changes in disk density structure to propogate inward is $t_{viscous} \sim t_{freefall}/\alpha$, where α is the disk viscosity parameter, with a value that is in the range $10^{-2} - 1$, and the freefall timescale is $t_{freefall} \simeq 1.9 \times 10^3 R_{11}^{3/2}$ s. A lag of the observed magnitude would occur if the X-rays affected the disk structure in such a way as to impede the reprocessing, for example by decreasing the disk scale height. If this occured a radius greater than that where most of the reprocessing occurs, then the lag would arise as a result of the inward propogation of the affected region; the propogation distance would be $\sim 10^{10}/\alpha$cm, comparable to the disk radius. The change in disk structure could be the result of X-ray ionization which ionizes or evaporates the outer disk layers. An alternative is that the X-rays affect the mass supply into the disk, which would occur if the mass transfer takes place as the result of an X-ray excited wind. However, the naive expectation for such a scenario is that it produces a positive feedback, which would produce positively correlated UV/X-ray variability, in contrast to what we observe.

Constraints on the density in the line forming regions come from the relative strengths of the various emission lines. From the doublet ratios we infer that the emitting gas must be at least marginally optically thick in the resonance lines of C IV and N V. The O IV λ1340, and O V λ1370 lines are subordinate lines, and so require either that the emitting ions be in an excited state, or that excitation occur from the ground state through a dipole-forbidden transition. The former case requires a combination of high gas density and optical depth in the resonance line leading to the level from which excitation can occur. This can be expressed as $n\tau \geq 10^{16}$ cm^{-3}. Such densities and optical depths are predicted to occur in X-ray heated disk atmospheres (Ko and Kallman, 1995).

The line profiles provide direct constraints on the dynamics in the emitting region. From Gaussian fits to the echelle spectra (Fig. 10) we infer that the gas velocity dispersion is less than the Keplerian speed expected at the outer disk edge. Fits to models for emission lines broadened by Kepler motion in an accretion disk require a somewhat contrived spacing for the two emission peaks expected from such a model, implying a lower Kepler velocity at the outer disk edge than would be predicted based on the other properties of the system. One scenario which might be consistent with the line profiles is emission in a turbulent region associated with the interaction of the accretion stream with the outer disk edge. If so, the line centroid energy would be expected to vary with orbital phase by an amount which reflects the orbital motion of the emission region about the center of mass of the system, and which could be as large as $\sim$100 km s^{-1}. Further observations with resolution comparable to those used here are needed to test this possibility.

If the blueshifts of the emission lines are due in part to orbital motion, then it is possible that the absorption line gas is associated with Sco X-1. However, the radial velocity curve of Crampton et al. (1976) suggest the systemic velocity is $\simeq$150 km s^{-1}, which is still greater than the absorption line velocities of 25-40 km s^{-1}. Since narrow UV absorption features are unlikely to be associated with gas falling into Sco X-1, we consider it most probable that the gas responsible for the absorption features is not associated with Sco X-1, either through its origins or its present dynamics. On the other had, on the basis of the data presented here we cannot rule out this possibility with certainty. The column densities implied by the C IV line strength is $N \simeq 2.6 \times 10^{16} \tau T_4^{1/2} x^{-1} \mathrm{cm}^{-2}$, where τ is the line center optical depth, T_4 is the gas temperature in units of 10^4 K, and x is the ion fraction. This is comparable to that expected from a bubble swept up by a wind with a speed 10^7 cm s^{-1} and a mass loss rate 10^{18} gm s^{-1} expanding into a medium with an ambient density of 1 cm^{-3} (Castor, McCray and Weaver 1975).

Acknowledgements: We thank M. Van der Klis, J. Swank, K. Mukai, J. Krolik and the referee for advice and useful suggestions. Support for this work was provided in part by a NASA grant through the Hubble Space Telescope Guest Investigator Program.

REFERENCES

Ake, T., 1996,,,private communication.

Begelman, M. C., McKee, C. F., and Shields, G.A., 1983, Ap. J., 271,70.

Begelman, M. C., and McKee, C.F., 1983, Ap. J., 271, 89.

Blandford, R. and McKee, C., 1982, Ap. J., 255, 419.

Bradshaw, C. F., Fomalont, E. B., and Geldzahler, B. J., 1997, Ap. J., 484, L55.

Canizares, C., et al., 1975, Ap. J., 197, 457.

Cordova, F.A., and Mason, K.O., 1982a, in,, Accretion Driven Stellar X-ray Sources, ed. W.H.G. Lewin and E. P. J. van den Heuvel , Cambridge University Press, Cambridge.

Cowley, A., and Crampton, D., 1975, Ap. J. Lett., 201, L65.

Cowley, A., 1976, in, Eighth Texas Symposium on Relativistic Astrophysics,, New York Academy of Sciences, M. D. Papagiannis, ed.

Crampton, D., Cowley, A., Hutchings, J.B., and Kaat, C., 1976, Astrophys. J., 207, 907.

Diplas, A., and Savage, B., 1994, Ap. J., 427; 274.

Done, C., and Krolik, J., 1996, Ap. J, 463, 144.

Eardley, D., Lightman, A., Payne, D., and Shapiro, S., 1978, Ap. J., 224, 53.

Edelson, R. and Krolik, J., 1988, Ap. J., 333, 646.

Frank, J., King, A., and Raine, D., 1985, 'Accretion Power in Astrophysics',,Cambridge University Press.

Giacconi, R. et al. 1962, Phys. Rev. Lett., 9, 439.

Gottlieb, E.W., Wright, E.L., and Liller, W., 1975, Ap. J. Lett., 195, L33.

Hartig, G., Crocker, J, Ford, H., 1993, SPIE, 1945, 17.

Hasinger, G., Priedhorsky, W. C., and Middleditch, J., 1989, Ap. J., 337, 843.

Howarth, I.D., and Wilson, R.E., 1983, M.N.R.A.S., 202, 347.

Kallman, T.R., and McCray, R. A., 1982, Ap. J. Supp., 50, 263.

Kallman, T.R., Vrtilek, S., and Raymond, J., 1991, Ap. J., 370, 717.

Kenyon, S., 1989,,,private communication .

Krolik, J. and Done, C., 1995, Ap. J., 440, 166.

Ko, Y., and Kallman, T.R., 1994, Ap. J., 431, 273.

Knude, J., 1987, Astr. Ap., 171, 289.

Leahy, D., et al., 1983, Ap. J, 266, 160.

Lewin, W., Van Paradijs, J.., and Van der Klis, M., 1989, Space Science Reviews, 46, 273.

London, R., 1982, in Cataclysmic Variables and Low Mass X-ray Binaries, J. Patterson and D. Lamb, eds.,.

London, R., McCray, R., and Auer, L., 1981, Ap. J., 243, 970.

Milgrom, M., 1976, Ap. J., 207, 902.

Morton, D., and Smith, W., 1973, Ap. J. Supp., 26, 333.

Press, W., Flannery, W., Teukolsky, S., and Vetterling, W., 1986, Numerical Recipes,, Cambridge University Press.

Priedhorsky, W., et al., 1986, Ap. J., 306, L91.

Raymond J.C., and Smith, B. H., 1977, Ap. J. Supp., 35, 419.

Ruderman, M., Shaham, J., and Tavani, M., 1989, Ap. J., 336, 507.

Savage, B.D., and Mathis, J.S., 1979, Ann. Rev. Ast. and Ap., 17, 73.

Schachter, J., Filippenko, A., V., and Kahn, S.M., 1989, Ap. J., 340, 1049.

Shakura, N.I., and Sunyaev, R.A., 1973, Astr. and Ap., 24, 337.

Sofia, S., Eichhorn, H., and Gatewood, G., 1969, A. J., 74, 1.

Vrtilek,S.D., Penninx, W., Raymond, J.C., Verbunt, F., Hertz, P., Wood, K., Lewin, W.H.G. and Mitsuda, K. 1991, ApJ, 376, 278. .

van der Klis et al., 1985, IAU Circ, 486,;.

van der Klis et al., 1996, Ap. J., 469,1;.

van der Klis et al., 1997, Ap. J., 481,97;.

Wade, R. A., 1984, M.N.R.A.S., 208, 381.

White, N.E., and Holt, S.S., 1982, Ap. J., 257, 318.

White, N.E. *et al.*, 1986, M.N.R.A.S., 218, 129.

White, N.E., Peacock, A., and Taylor, B.G. 1985, Ap. J., 296, 475.

White, N.E., Stella, L., and Parmar, A., 1988, Ap. J., 324, 363.

Willis, A., et al., 1980, Ap. J., 237, 596.

Table 1

Journal of Observations

interval	Instrument	Start (UT)	Stop (UT)	$\lambda_{min}(\AA)$	$\lambda_{max}(\AA)$
1	GHRS G140L RAPID	50142.80780448	50142.81888521	1260	1550
2	GHRS G140L RAPID	50142.82586003	50142.83725326	1260	1550
3	GHRS G160M ACCUM	50142.74333833	50142.77154290	1210	1260
4	GHRS G160M ACCUM	50142.68090778	50142.74224169	1530	1570
5	GHRS G160M ACCUM	50142.61785222	50142.67916298	1205	1235
6	GHRS echelle A ACCUM	50142.87574574	50142.90646767	1236	1244
7	GHRS echelle A ACCUM	50142.94247028	50142.97319221	1545	1555
8	XTE	50142.800781250	50142.840824074	12.4	0.62

Table 2

Gaussian line fits

obs	λ (Å)	$F_{\rm line}$ (erg cm^{-2} s^{-1})	$F_{\rm continuum}$ (erg cm^{-2} s^{-1} Å^{-1})	W (Å)	EW (Å)
G140L 1	1370	1.08E-12±4.03E-14	2.48E-13±1.38E-14	20.7	4.3±0.3
G140L 1	1395	2.73E-12±2.98E-14	2.24E-13±1.21E-14	31.5	12.2±0.7
G140L 1	1549	2.73E-12±2.98E-14	2.24E-13±1.23E-14	31.5	12.2±0.7
G140L 1	1341	3.87E-12±4.67E-14	1.81E-13±3.77E-14	7.4	21.4±4.5
G140L 1	1480	3.87E-12±4.67E-14	1.81E-13±3.42E-14	7.4	21.4±4.1
G140L 1	1500	4.09E-13±6.22E-14	2.71E-13±6.80E-15	9.8	1.5±0.2
G140L 2	1370	8.86E-13±3.14E-14	1.93E-13±1.08E-14	20.7	4.6±0.3
G140L 2	1395	2.36E-12±2.32E-14	1.75E-13±9.93E-15	31.5	13.5±0.8
G140L 2	1549	2.36E-12±2.32E-14	1.75E-13±9.98E-15	31.5	13.5±0.8
G140L 2	1341	3.39E-12±3.64E-14	1.41E-13±3.73E-14	7.4	24.1±6.4
G140L 2	1480	3.39E-12±3.64E-14	1.41E-13±2.90E-14	7.4	24.1±5.0
G140L 2	1500	3.27E-13±4.95E-14	2.10E-13±5.52E-15	9.2	1.6±0.2

Table 3

Gaussian line fits

line	instrument	$v_{\rm emiss}$ (km/s)	$W_{\rm emis}$ (km/s)	$EW_{\rm emis}$ (Å)	v_{abs} (km/s)	$W_{\rm abs}$ (km/s)	$EW_{\rm abs}$ (Å)	χ^2/ν
C IV	G160M	$-77.9^{+11.6}_{-1.9}$	$349^{+0.3}_{-1.4}$	$23.5^{+2.3}_{-0.7}$	$-27.5^{+0}_{-19.4}$	$38.6^{+23.8}_{-0.5}$	$1^{+0.6}_{-0.3}$	2263/2000
	ech	$-132^{+9.7}_{-7.8}$	$274^{+7.1}_{-7.4}$	$24.2^{+3.5}_{-3.1}$	$-37.2^{+5.8}_{-3.9}$	$46.5^{+0.1}_{-2.2}$	$1.6^{+0.2}_{-0.2}$	1612/2000
N V	G160M	$-177^{+7.3}_{-4.8}$	$354^{+5.3}_{-5.3}$	$23.1^{+1.5}_{-1.3}$	$-34.1^{+55.7}_{-12.1}$	$45^{+28}_{-30.1}$	$0.2^{+0.2}_{-0.2}$	7984/2000
	ech	$-117^{+0}_{-60.6}$	$246^{+20.7}_{-0.7}$	$13.1^{+2.1}_{-4.2}$	$-26.9^{+2.4}_{-19.4}$	$31.4^{+25.1}_{-0.7}$	$0.5^{+0.9}_{-0}$	2595/2000

Table 4

disk line model fits

line	instrument	$v_{\rm emiss}$ (km/s)	$W_{\rm emis}$ (km/s)	$EW_{\rm emis}$ ($\AA$)	$v_{\rm abs}$ (km/s)	$W_{\rm abs}$ (km/s)	$EW_{\rm abs}$ ($\AA$)	χ^2/ν
C4	ech	-116.7	$387.7^{+106.3}_{-120.8}$	$66.5^{+8.8}_{-19.8}$	$-39.1^{+3.9}_{-1.9}$	$43.3^{+3.2}_{-3}$	$2^{+0.3}_{-0.3}$	1915/2000
n5	ech	-102	$484.5^{+217.8}_{-239.2}$	$29.7^{+11.1}_{-16.4}$	$-31.7^{+300}_{-300.6}$	$24.2^{+13}_{-0.3}$	$0.7^{+0.4}_{-0.1}$	3207/2000

Figure Captions

Figure 1 Time averaged spectra taken by the G140L grating during the two intervals of observation, corresponding to those described in table 1. Upper panel shows first interval, second panel shows second interval. Fluxes are in units of erg cm^{-2} s^{-1} $\AA^{-1}$. The bottom panel show the logarithm of the ratio of the two intervals.

Figure 2 The series from the G140L RAPID mode observations and from XTE. Vertical axis is counts per 0.1 s time bin. Horizontal axis is time relative to the start of the X-ray observation.

Figure 3 Power spectra in the 3 energy bands corresponding to figure 2.

Figure 4 Autocorrelation functions for the time series in the 3 energy bands corresponding to figure 2.

Figure 5 Cross correlation functions between the time series in the 3 energy bands corresponding to figure 2.

Figure 6 Simulated cross correlation functions between the time series in the 3 energy bands corresponding to figure 2.

Figure 7 Response function calculated using the regularized linear inversion algorithm. Units of response are s^{-1}.

Figure 8 Echelle spectrum in the vicinity of the C IV line (crosses). Data has been binned into 1 $\AA$ bins, and the error bars reflect the dispersion about the mean value of the data within that bin. Solid curve is best fit disk line spectrum. Fluxes are in units of erg cm^{-2} s^{-1} $\AA^{-1}$.

Figure 9 Echelle spectrum in the vicinity of the N V line (crosses). Data has been binned into 1 $\AA$ bins, and the error bars reflect the dispersion about the mean value of the data within that bin. Solid curve is best fit disk line spectrum. Fluxes are in units of erg cm^{-2} s^{-1} $\AA^{-1}$.

Figure 10 G160M spectrum in the vicinity of the Lα line (crosses). Solid curve is best fit damped absorption line spectrum plus a narrow gaussian emission. Fluxes are in units of erg cm^{-2} s^{-1} $\AA^{-1}$.

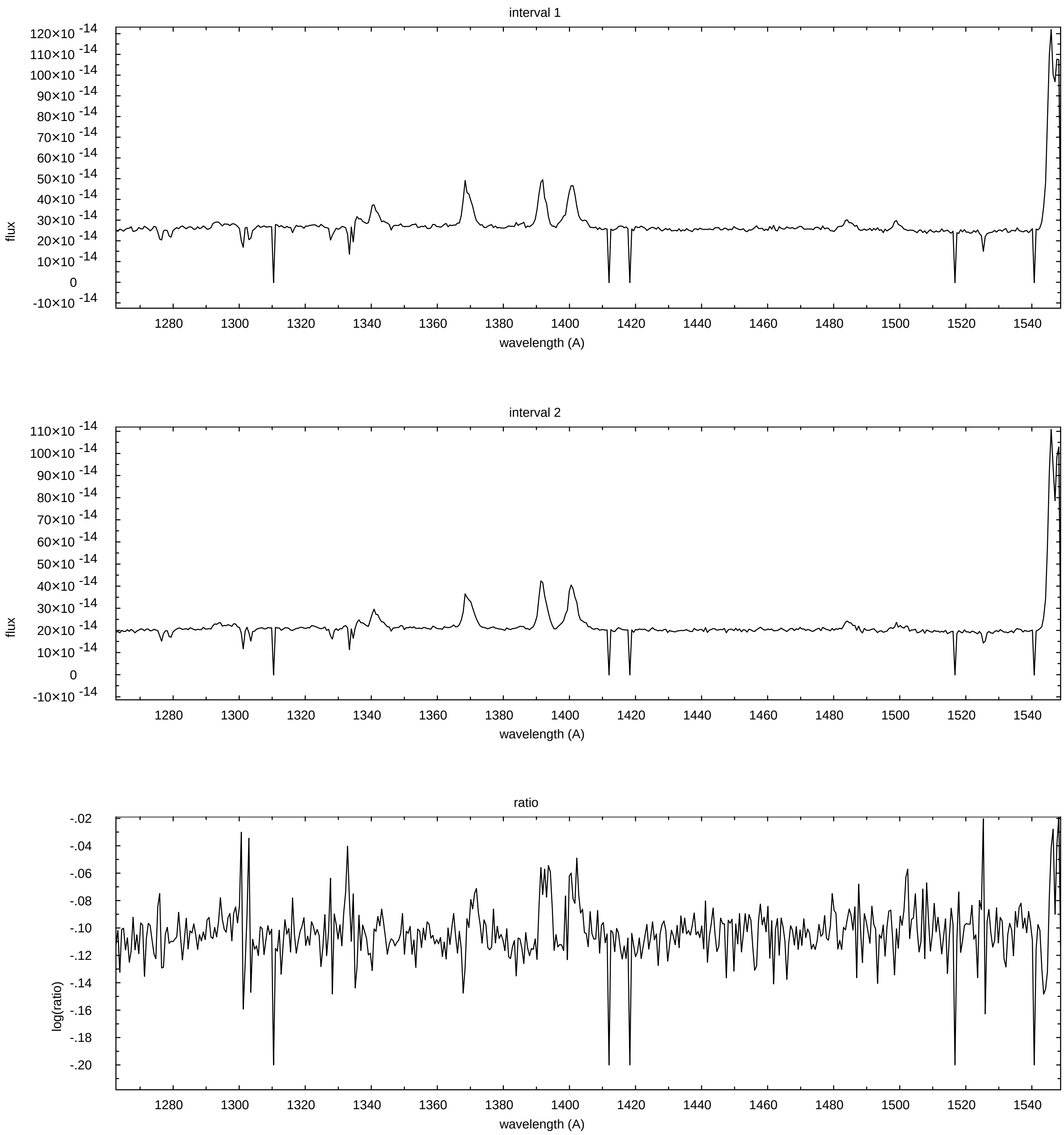
interval 1
flux
120×10 -14
110×10 -14
100×10 -14
90×10 -14
80×10 -14
70×10 -14
60×10 -14
50×10 -14
40×10 -14
30×10 -14
20×10 -14
10×10 -14
0
-10×10 -14
1280
1300
1320
1340
1360
1380
1400
1420
1440
1460
1480
1500
1520
1540
wavelength (A)
interval 2
flux
110×10 -14
100×10 -14
90×10 -14
80×10 -14
70×10 -14
60×10 -14
50×10 -14
40×10 -14
30×10 -14
20×10 -14
10×10 -14
0
-10×10 -14
1280
1300
1320
1340
1360
1380
1400
1420
1440
1460
1480
1500
1520
1540
wavelength (A)
ratio
log(ratio)
-.02
-.04
-.06
-.08
-.10
-.12
-.14
-.16
-.18
-.20
1280
1300
1320
1340
1360
1380
1400
1420
1440
1460
1480
1500
1520
1540
wavelength (A)

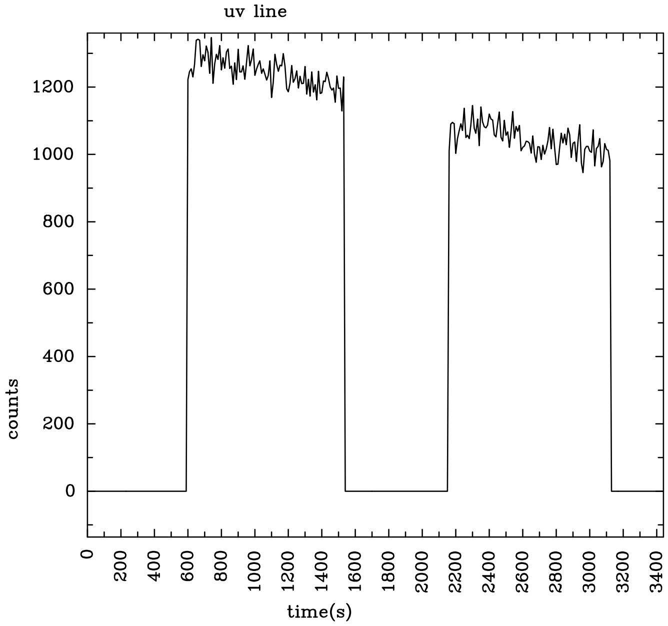
uv line
counts
time(s)
0
200
400
600
800
1000
1200
1400
1600
1800
2000
2200
2400
2600
2800
3000
3200
3400

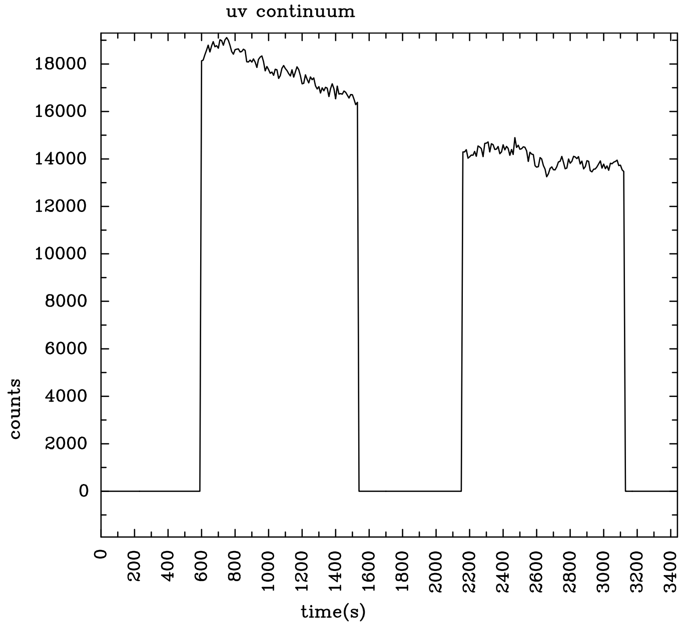
uv continuum
counts
time(s)
0
2000
4000
6000
8000
10000
12000
14000
16000
18000

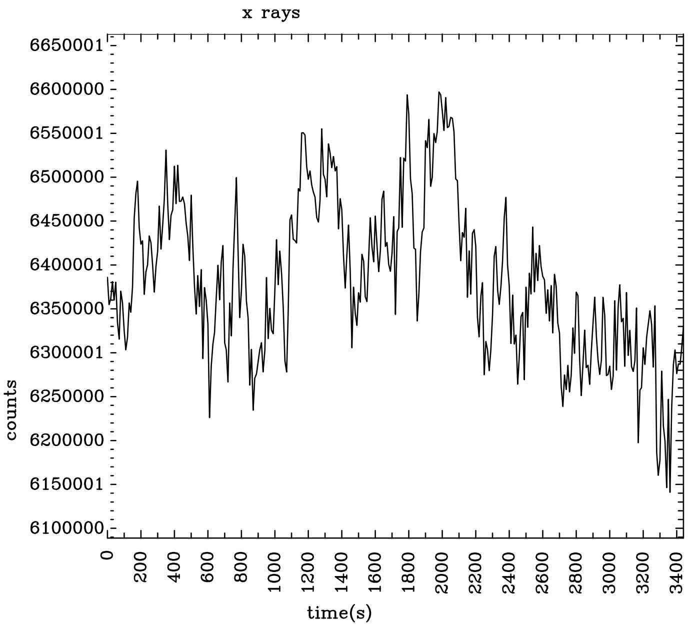
x rays
counts
time(s)
6100000
6150001
6200000
6250000
6300001
6350000
6400001
6450000
6500000
6550001
6600000
6650001

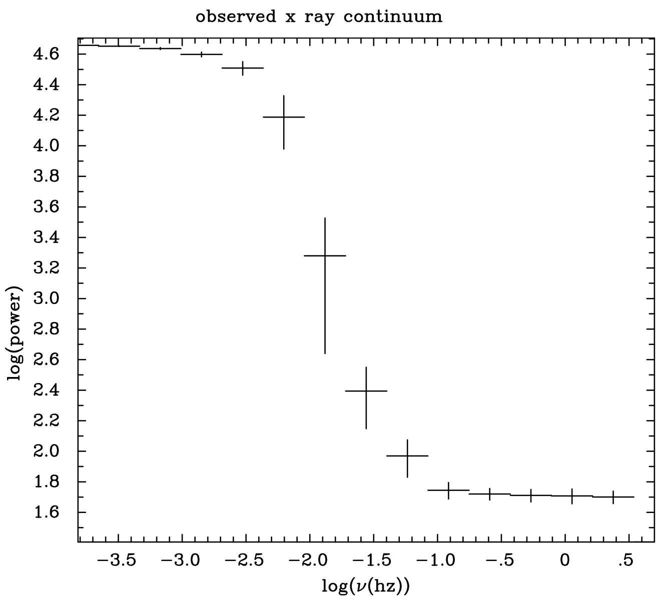
observed x ray continuum
log(power)
4.6
4.4
4.2
4.0
3.8
3.6
3.4
3.2
3.0
2.8
2.6
2.4
2.2
2.0
1.8
1.6
−3.5
−3.0
−2.5
−2.0
−1.5
−1.0
−.5
0
.5
log(ν(hz))

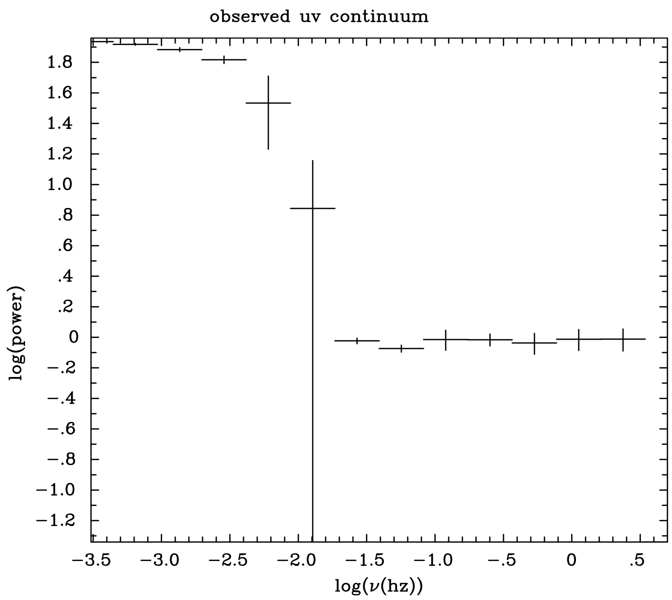
observed uv continuum
log(power)
1.8
1.6
1.4
1.2
1.0
.8
.6
.4
.2
0
−.2
−.4
−.6
−.8
−1.0
−1.2
−3.5
−3.0
−2.5
−2.0
−1.5
−1.0
−.5
0
.5
log(ν(hz))

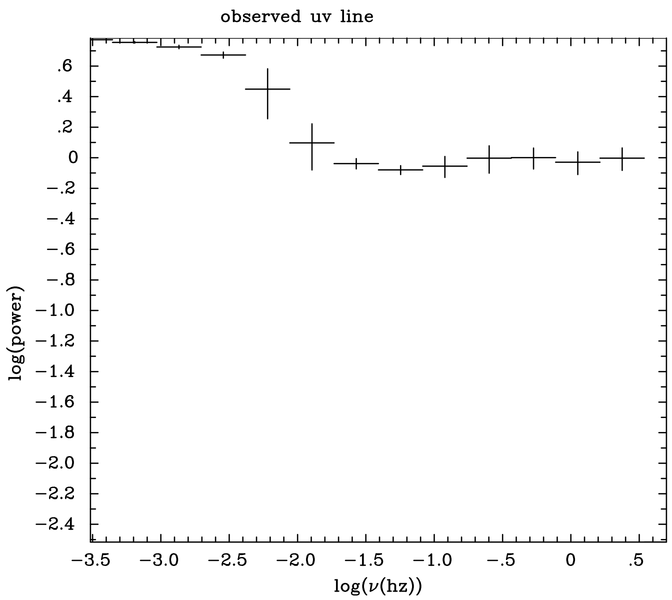
observed uv line
log(power)
.6
.4
.2
0
−.2
−.4
−.6
−.8
−1.0
−1.2
−1.4
−1.6
−1.8
−2.0
−2.2
−2.4
−3.5
−3.0
−2.5
−2.0
−1.5
−1.0
−.5
0
.5
log(ν(hz))

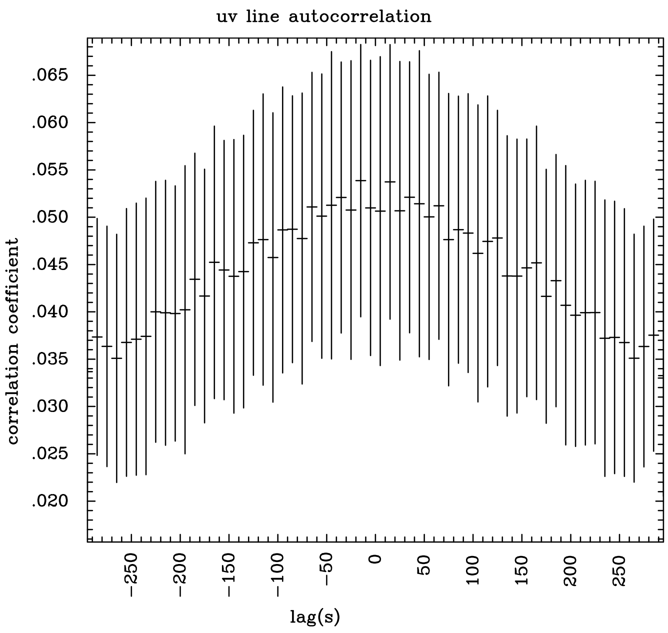
uv line autocorrelation
correlation coefficient
.020
.025
.030
.035
.040
.045
.050
.055
.060
.065
−250
−200
−150
−100
−50
0
50
100
150
200
250
lag(s)

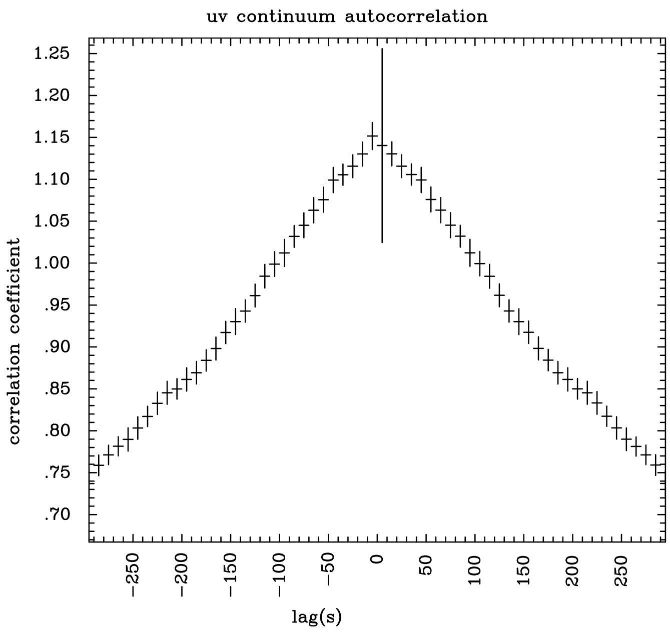
uv continuum autocorrelation
correlation coefficient
.70
.75
.80
.85
.90
.95
1.00
1.05
1.10
1.15
1.20
1.25
−250
−200
−150
−100
−50
0
50
100
150
200
250
lag(s)

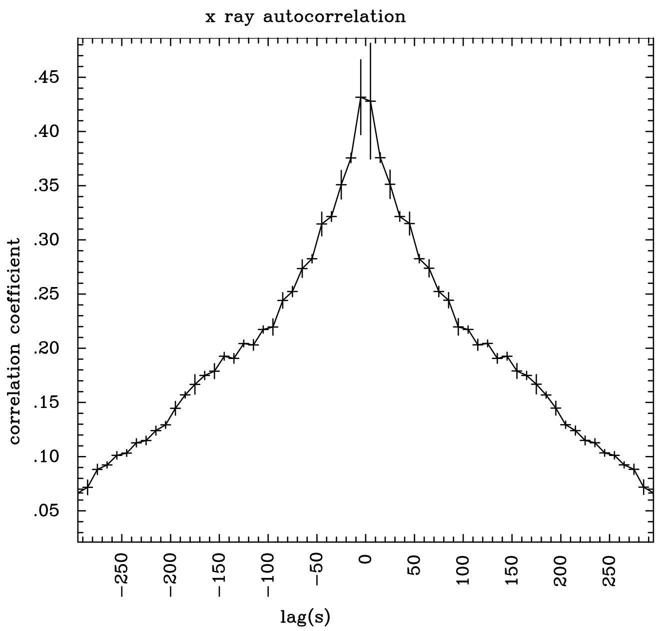
x ray autocorrelation
correlation coefficient
.05
.10
.15
.20
.25
.30
.35
.40
.45
−250
−200
−150
−100
−50
0
50
100
150
200
250
lag(s)

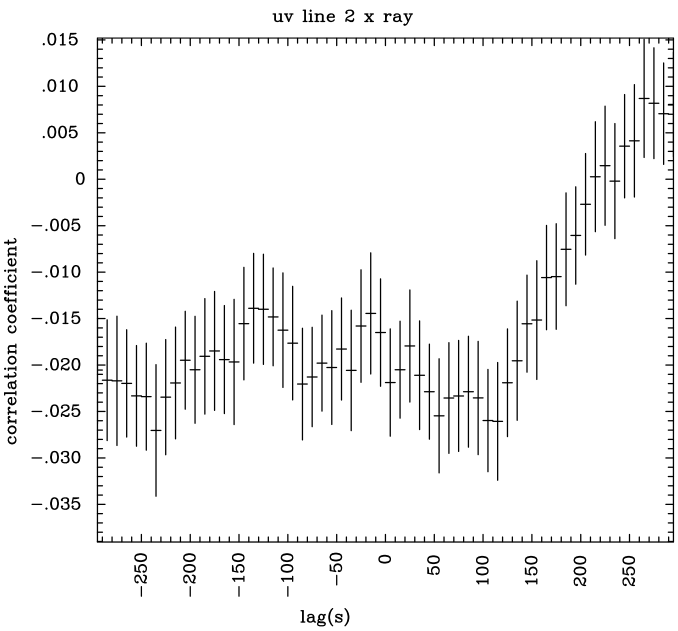
uv line 2 x ray
correlation coefficient
lag(s)
.015
.010
.005
0
−.005
−.010
−.015
−.020
−.025
−.030
−.035
−250
−200
−150
−100
−50
0
50
100
150
200
250

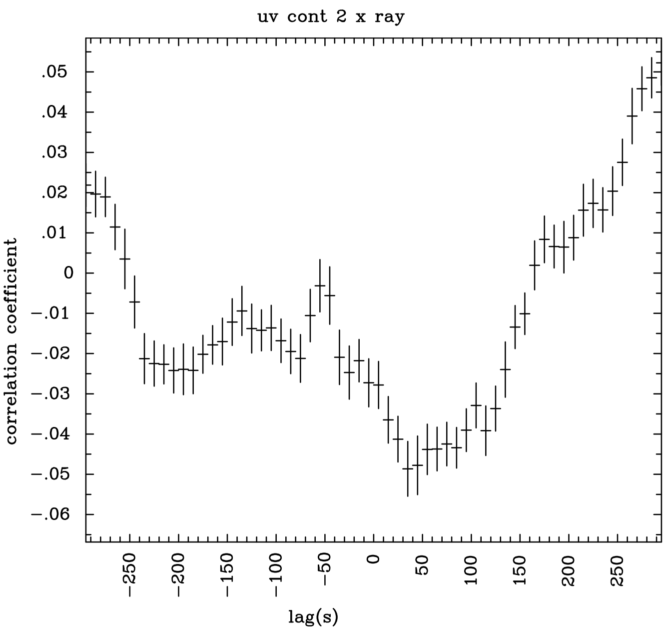
uv cont 2 x ray
correlation coefficient
lag(s)
.05
.04
.03
.02
.01
0
−.01
−.02
−.03
−.04
−.05
−.06
−250
−200
−150
−100
−50
0
50
100
150
200
250

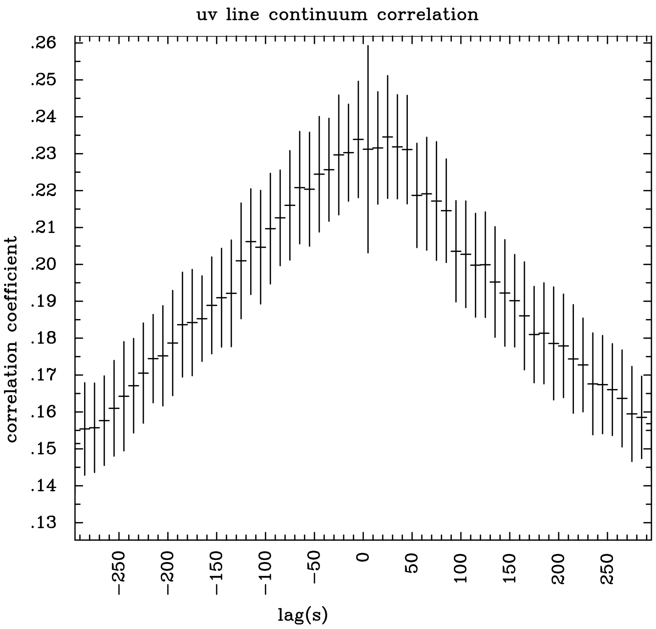
uv line continuum correlation
correlation coefficient
lag(s)
.26
.25
.24
.23
.22
.21
.20
.19
.18
.17
.16
.15
.14
.13
−250
−200
−150
−100
−50
0
50
100
150
200
250

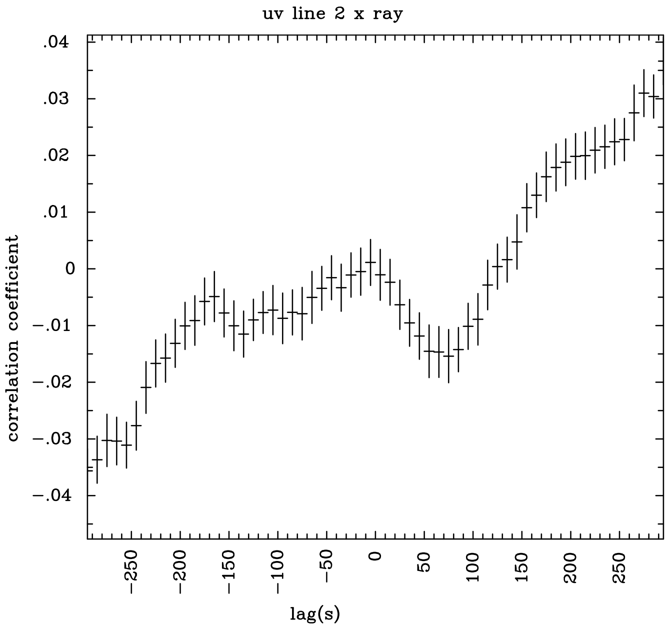
uv line 2 x ray
correlation coefficient
.04
.03
.02
.01
0
-.01
-.02
-.03
-.04
-250 -200 -150 -100 -50 0 50 100 150 200 250
lag(s)

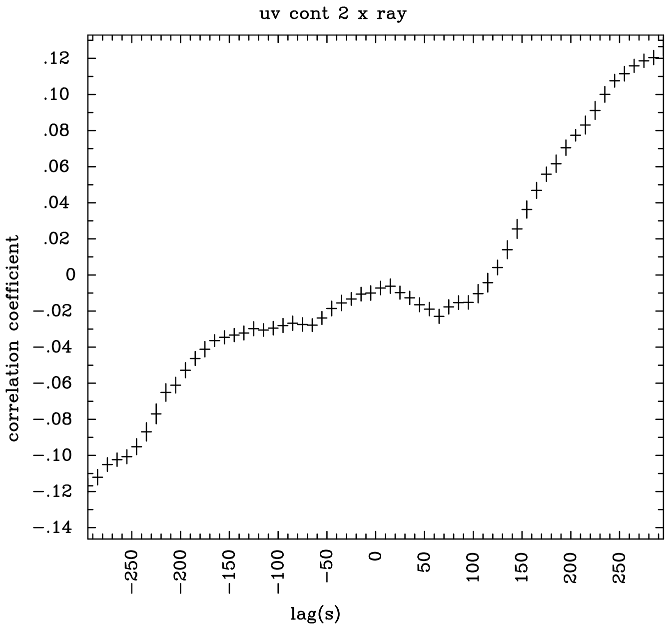
uv cont 2 x ray
correlation coefficient
.12
.10
.08
.06
.04
.02
0
-.02
-.04
-.06
-.08
-.10
-.12
-.14
-250 -200 -150 -100 -50 0 50 100 150 200 250
lag(s)

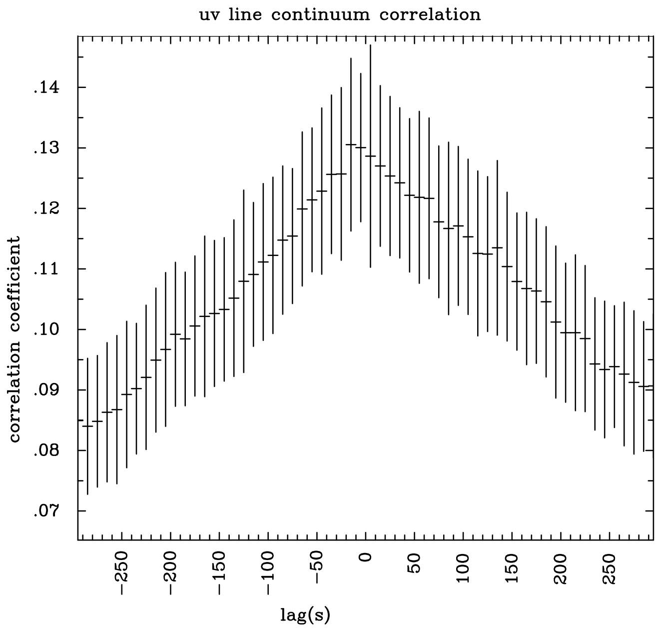
uv line continuum correlation
correlation coefficient
.14
.13
.12
.11
.10
.09
.08
.07
-250 -200 -150 -100 -50 0 50 100 150 200 250
lag(s)

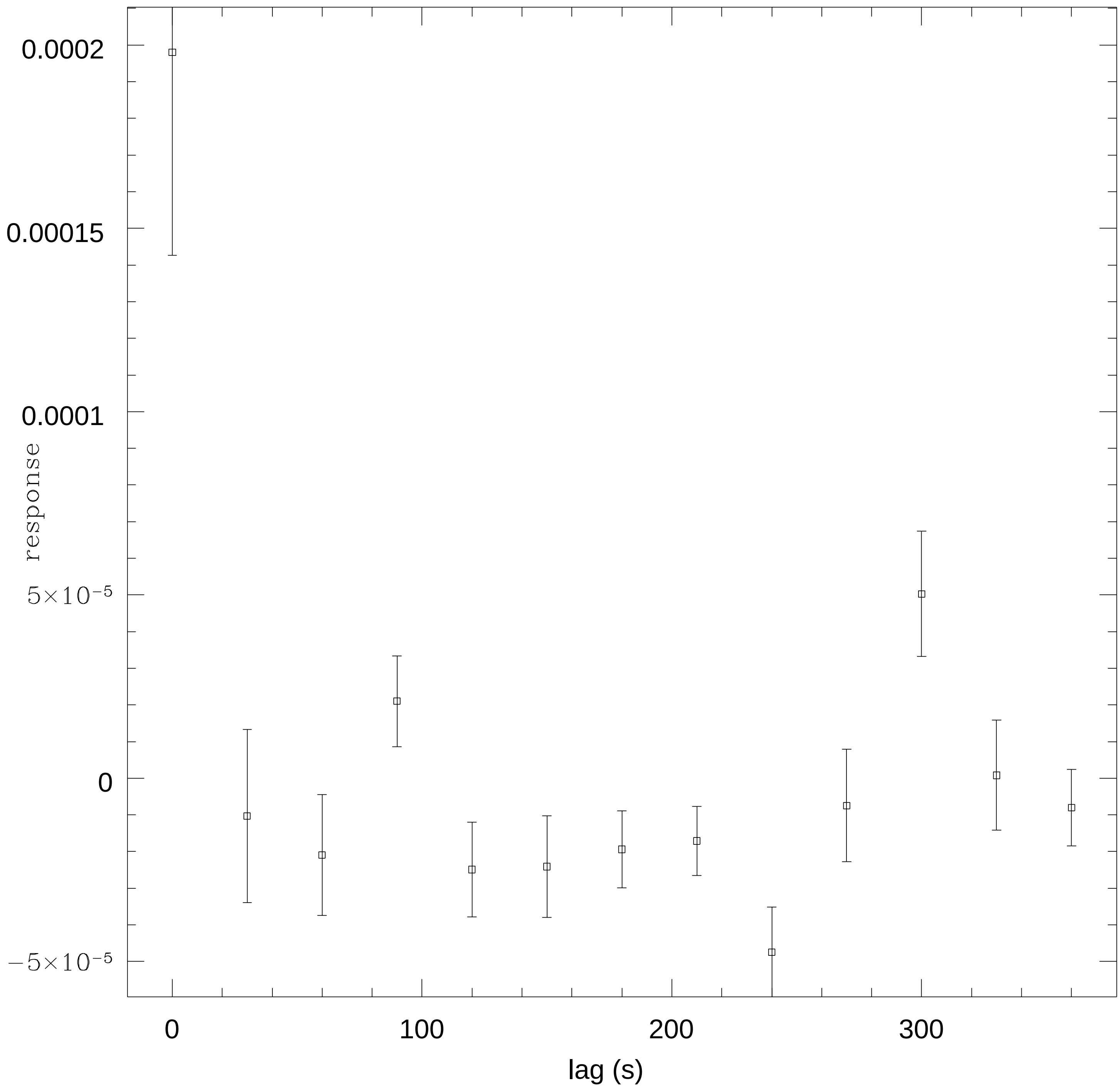
0.0002
0.00015
0.0001
5×10⁻⁵
0
−5×10⁻⁵
response
0
100
200
300
lag (s)

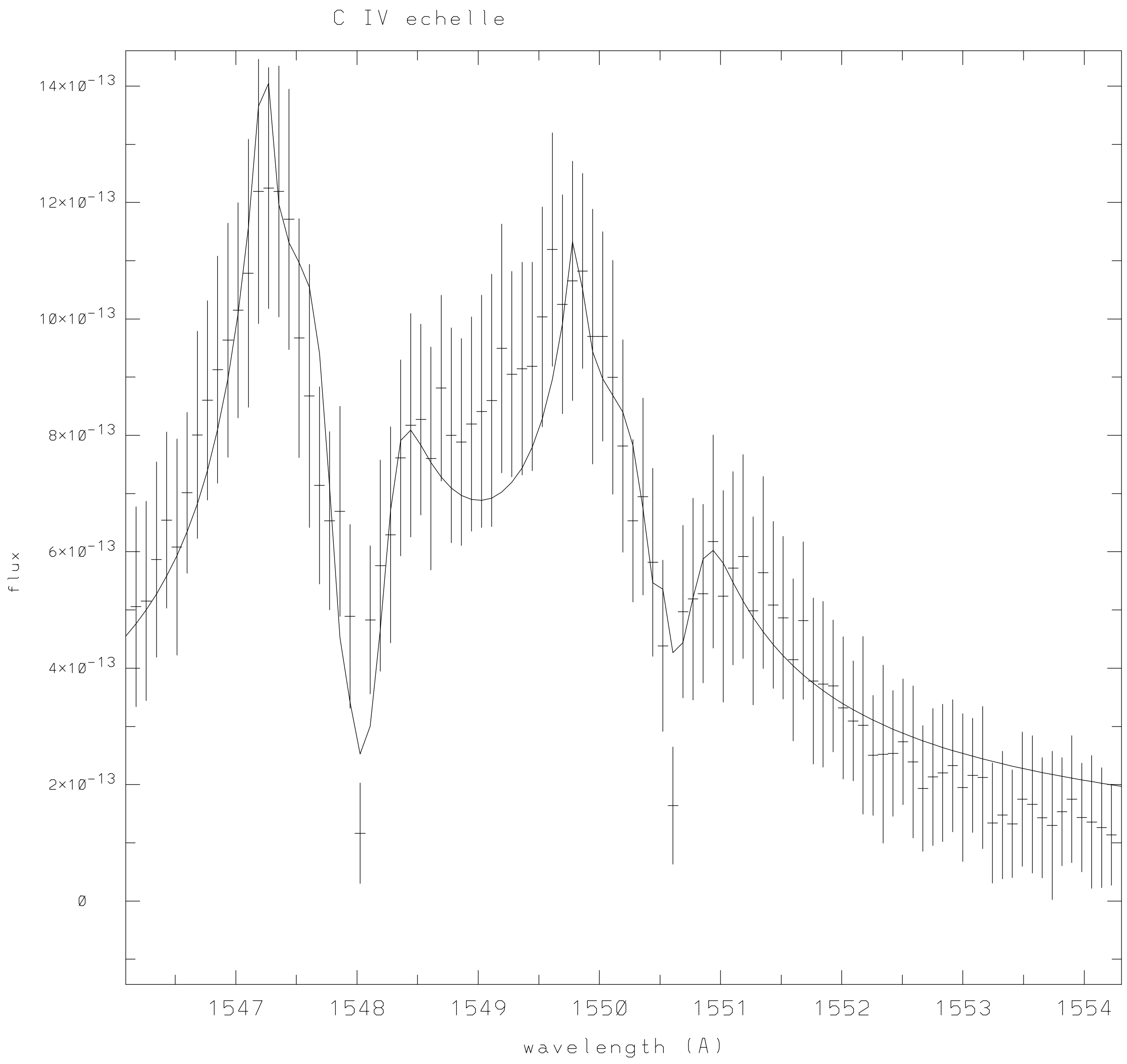
C IV echelle
14×10^{-13}
12×10^{-13}
10×10^{-13}
8×10^{-13}
6×10^{-13}
4×10^{-13}
2×10^{-13}
0
flux
1547
1548
1549
1550
1551
1552
1553
1554
wavelength (A)

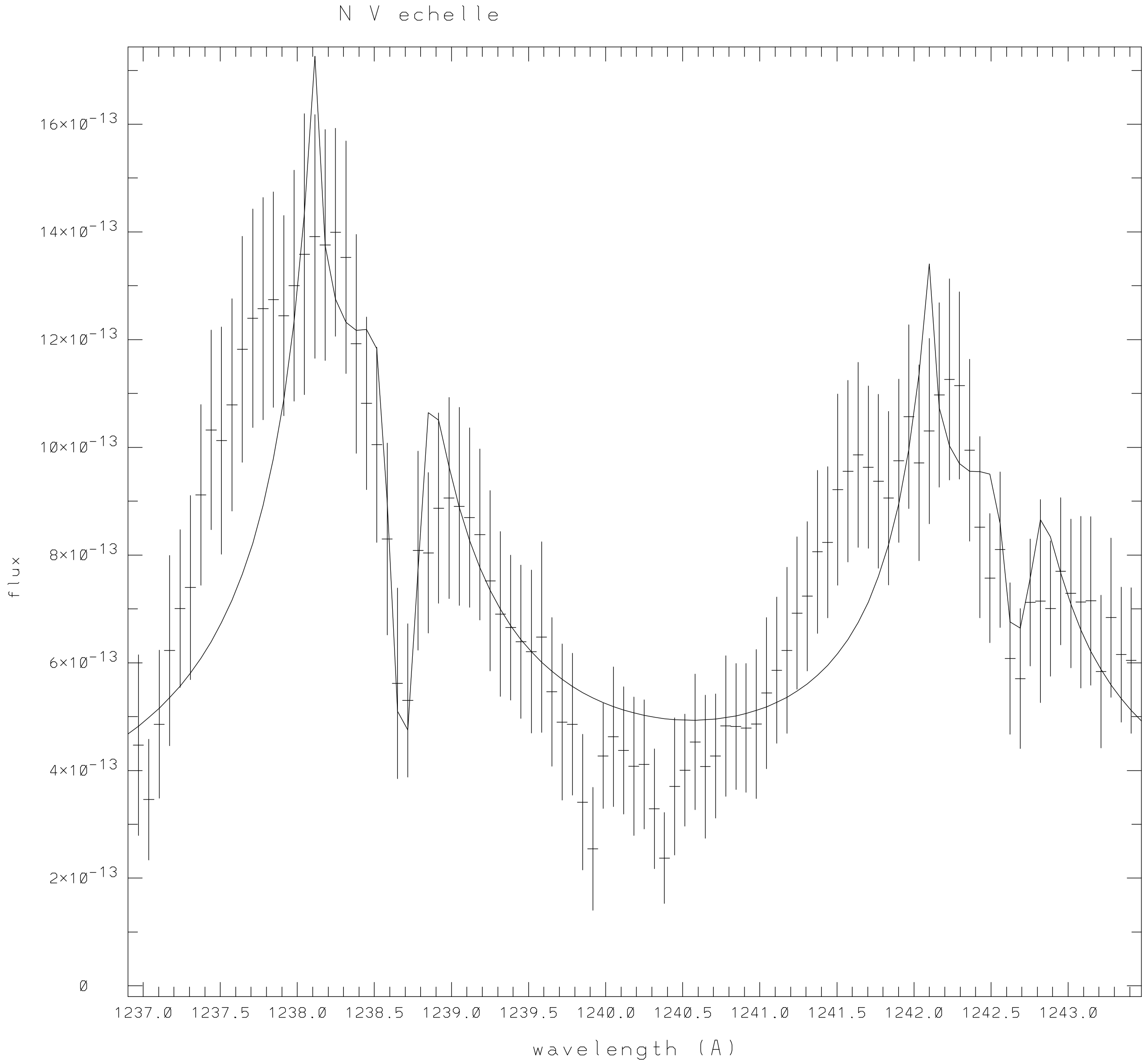
N V echelle
flux
wavelength (A)
16×10^{-13}
14×10^{-13}
12×10^{-13}
10×10^{-13}
8×10^{-13}
6×10^{-13}
4×10^{-13}
2×10^{-13}
0
1237.0
1237.5
1238.0
1238.5
1239.0
1239.5
1240.0
1240.5
1241.0
1241.5
1242.0
1242.5
1243.0

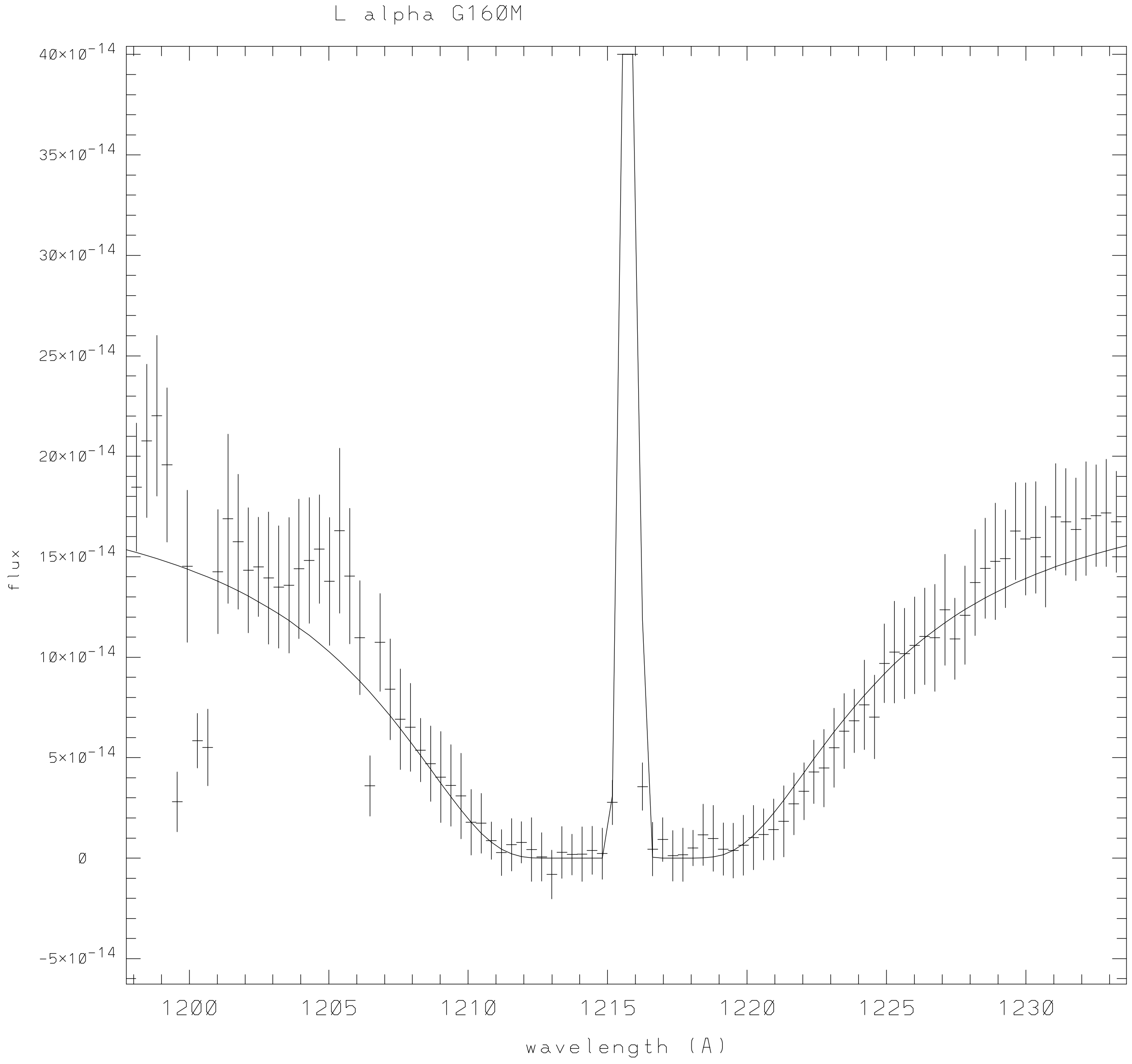
L alpha G160M
flux
wavelength (A)
40×10^-14
35×10^-14
30×10^-14
25×10^-14
20×10^-14
15×10^-14
10×10^-14
5×10^-14
0
-5×10^-14
1200
1205
1210
1215
1220
1225
1230